Published in final edited form as:
Trends Biomater Artif Organs. 2012 ; 26(2): 74–85.

Electro and Magneto-Electropolished Surface Micro-Patterning on Binary and Ternary Nitinol

Dharam Persaud-Sharma[1], **Norman Munroe**[2], and **Anthony McGoron**[3]

Dharam Persaud-Sharma: Dpers001@fiu.edu; Norman Munroe: munroen@fiu.edu; Anthony McGoron: mcgorona@fiu.edu

[1]Florida International University, Department of Biomedical Engineering, 10555 W. Flagler Street, Miami, FL 33199, USA

[2]Florida International University, Department of Mechanical & Materials Engineering, 10555 W. Flagler Street, Miami, FL 33199, USA

[3]Florida International University, Department of Biomedical Engineering, 10555 W. Flagler Street, Miami, FL 33199, USA

Abstract

In this study, an Atomic Force Microscopy (AFM) roughness analysis was performed on non-commercial Nitinol alloys with Electropolished (EP) and Magneto-Electropolished (MEP) surface treatments and commercially available stents by measuring Root-Mean-Square (RMS), Average Roughness (Ra), and Surface Area (SA) values at various dimensional areas on the alloy surfaces, ranging from (800 × 800 nm) to (115 × 115μm), and (800 × 800 nm) to (40 × 40 μm) on the commercial stents. Results showed that NiTi-Ta 10 wt% with an EP surface treatment yielded the highest overall roughness, while the NiTi-Cu 10 wt% alloy had the lowest roughness when analyzed over (115 × 115 μm). Scanning Electron Microscopy (SEM) and Energy Dispersive Spectroscopy (EDS) analysis revealed unique surface morphologies for surface treated alloys, as well as an aggregation of ternary elements Cr and Cu at grain boundaries in MEP and EP surface treated alloys, and non-surface treated alloys. Such surface micro-patterning on ternary Nitinol alloys could increase cellular adhesion and accelerate surface endothelialization of endovascular stents, thus reducing the likelihood of in-stent restenosis and provide insight into hemodynamic flow regimes and the corrosion behavior of an implantable device influenced from such surface micro-patterns.

Keywords

AFM; Nano-indentation; EDS/SEM; NiTi; Surface Roughness; Electropolishing

1. Introduction

In endovascular therapy, several types of treatments exist for alleviating health complications in patients who suffer from vascular diseases. As such, there is a continuous need for new and improved biomaterials and treatment processes to maximize its effectiveness and minimize any deleterious effects. The bulk properties of a material are contributory criteria in its selection for a particular application, while the interfacial surfaces of a material within a given environment elicit a more immediate biological response [1-3].

Correspondence to: Dharam Persaud-Sharma, Dpers001@fiu.edu.

The alloy Nitinol (NiTi) is a material commonly used for the manufacturing of peripheral stents which has recently been considered for the application of cardiovascular stents because of its corrosion resistance, biocompatibility, and shape-memory characteristic [4-5]. Varying Ni and Ti compositions result in an alloy with the ability to retain a particular shape and recover from deformation due to applied stress or temperatures as high as 10% from its equilibrium conditions [6]. Nitinol is ideally suited for endovascular treatments because of its self-expanding capability, which eliminates the need for post-deployment heating for device positioning. However, because of the potential for high Ni ion leaching from NiTi with its cytotoxic effects on cells, ternary NiTi-X alloys are being explored with the aim to reduce Ni ion leaching while retaining super-elastic properties inherent to shape-memory alloys such as NiTi [7]. An example of a ternary alloy worth consideration is NiTiCu. It has been documented that the addition of Cu to binary NiTi results in good corrosion resistance, narrow transformation hysteresis, and Ti_3Ni_4 precipitation [8-10], which helps to stabilize its super-elastic characteristics. Tantalum, a highly radiopaque metal, has been added to binary Nitinol to enable better visualization of the material under fluoroscopic, X-ray, MR imaging, and computed tomography (CT) [11-13]. Highly passivating elements like Chromium have been added to NiTi in order to improve corrosion resistance [14]. Nitinol was once considered to possess superior adaptability to vessel conformation;however, ternary Nitinol alloys have since demonstrated both superior adaptability and biocompatibility [12, 15]. Ion leaching is an important contributory factor to a coronary stents biocompatibility, and Ni ion leaching from NiTi *in vivo* is dependent upon the surface finishing quality and technique utilized [16].

Two recently explored techniques to enhance surface quality and deburr surface defects produced from the manufacturing process are: Electropolishing (EP) and Magneto-electropolishing (MEP) [17]. Electropolishing is a process that is particularly important for the manufacturing of medical devices, because it has been shown to improve corrosion resistance, biocompatibility, mechanical performance (fatigue/fracture), wear/tribological properties, and overall visual appearance [18]. MEP is a similar type of surface treatment, except that a magnetic field is applied during the electropolishing process [19]. In this technique, the strength of the magnetic field serves to either increase or decrease the dissolution rate of the processed material. However, the dissolution rate is also dependent on the type of electrolyte used as well as the inherent magnetic properties of the material being dissolved [20, 21].

Encouraging research has supported EP and MEP surface treatments toward the application on such alloys used for endovascular treatment because of its ability to create a uniform and stable passive film with a preferred low nickel ion concentration on the surface of the sample, and by shifting corrosion potentials into the direction of greater corrosion resistance [19, 22- 23].

Surface roughness is a contributory factor to the biocompatibility of a material as governed by its *in vivo* corrosion behavior. Rougher surfaces tend to increase corrosion rates, thereby eluting ions into the implantable environment. Increased ion leaching such as Ni can be toxic to the implantable environment and host [16]. Smoother finished surfaces decrease the likelihood of platelet adhesion and thrombus formation, thus reducing major post-treatment risks of in-stent restenosis [12]. On the contrary, research has shown that surface modifications which induce grooves or macroscopically significant elevations on the surface of a material can increase the rate of endothelialization, which has also been shown to reduce in-stent restenosis and thrombosis [21, 30- 32]. Recently, *in-vitro* studies based upon rat aortic endothelial cell adhesion and elongation has demonstrated an enhanced growth of the cells on patterned Poly-dimethyl siloxane (PDMS) surfaces, with a minimum threshold width spacing of 100 nm, and an increased nano-scaled surface roughness [24]. This

demonstrates that highly micro-patterned surfaces enhance the degree of endothelial cell adhesion, reducing post-implantation risks of in-stent restenosis and thrombus formations [24, 30-32].

In this study, several ternary NiTi alloys with and without EP and MEP surface treatments were analyzed using AFM techniques over various scan sizes to evaluate roughness at the micron and nano-scale levels. SEM techniques revealed morphology characteristics which were compared with AFM data. Investigating the mechanical and interfacial properties of such ternary NiTi alloys at the nanometer and micrometer-level provides information as to the influence of surface roughness on protein adsorption, cellular adhesion, and corrosion behavior [25]. This can provide insight into clinically relevant in-stent restenosis, thrombocyte adhesion sites, and leaching of Ni ions due to corrosion.

2. Materials and Methods

The addition of a third element to Nitinol enhances certain desirable mechanical properties such as Young's Modulus and Surface Hardness, while preserving the shape-memory characteristic. All binary and ternary Nitinol alloys (NiTi, NiTiCr-10 wt%, NiTiCu-10 wt%, NiTiTa-10 wt%) used in this study were manufactured by an Arc-Melting method at the National Institute of Standards and Technology (NIST) material science and engineering laboratory. Patented and proprietary commercial MEP and EP surface treatments were performed by ElectroBright ® (Macungie, PA, USA). The Nitinol stents that were obtained from a commercial source were prepared for nanoindentation studies by mounting them in an epoxy resin mold using Buehler Buehlermet II Epothin resin, hardener, and release agent. The surface of the mold was then polished using wet [320,400,600] Buehler Buehlermet II Silicon Carbide Abrasive paper. Fine comb polishing was also performed using Buehler Metadi Monocrystalline Diamond suspensions of 9, 6, and 1μm, respectively.

Two commercially available endovascular Nitinol stents (UNC-1, COL-1) were also studied for comparison with the ternary and binary alloys, as they are representative of deliverable commercial products readily used in the health care industry. All of the ternary and binary alloys were analyzed as-received, within their martensitic phase and were ultrasonically cleaned in acetone using a Branson ultrasonic cleaner, rinsed with distilled water, and dried with N_2 gas before any testing.

Surface hardness (SH) and Young's Modulus (YM) for these stents were determined using a Hysitron Nanoindenter system with a diamond Berkovich 3-face tip of with a radius of 100 nanometers. A normal load of 2000 μN was applied, with a loading/unloading rate of 200 μN/s. A 3 second dwell at peak loads was also applied. During tribometeric testing of the commercial stents, a normal applied load of 1200 μN was used, as well as an applied loading and unloading rate of 120 μN/s. The binary NiTi alloy was used as a reference from which to assess the effect of the addition of the ternary element to Nitinol.

Scanning Electron Microscopy (SEM) coupled with Energy Dispersive X-ray Spectroscopy (EDS) analyses on all samples was conducted using a JEOL JSM 5900LV and EDS-UTW Detector system. Images were also analyzed in both secondary electron imaging and backscatter imaging modes at an accelerating voltage of 20 KeV.

2.1 AFM Analysis

In this study, a VEECO Nanoscope IIIa Multimode AFM was utilized. The cantilevers used in this investigation were BudgetSensors Tap300Al-G, equipped with an aluminum reflex coating. These cantilevers have a resonant frequency of 300 KHz +/- 100 KHz that is utilized in the tapping frequency mode. The tip radius was less than 10 nm, and had a tip

height of 17 μm ± 2 μm. The frequency of oscillation was often optimized in order to obtain the most accurate information. Images were mostly obtained with a resolution of 256 × 256 pixels, and high resolution images were obtained for 3-dimensional visualization at 512 × 512 pixels. The scan frequency was often changed depending on the topographical features of the sample. The post-image processing of the data was obtained using NanoScope 5.3r1 software.

AFM images were obtained within the following dimensions: size I (10 × 10 μm), size II (5 × 5 μm), size III (115× 115μm), and size IV (800 × 800 nm). A minimum of 5 images were collected from sizes I and III, and 10 images for size ranges II and IV. More images were selected from the latter, because the surface artifacts on the alloys were within those dimensions. Size III provided an overall perspective of the surface by revealing any surface patterns or grooves, whereas, size IV provided finer topographic details that are pertinent at the substrate-cellular interface level. Height differences between the highest and lowest points in a scan area (Rmax) were gathered for scan size III to evaluate the height difference between grain surfaces and grain boundary regions. All images were acquired in a non-contact tapping mode; a mode in which the tip oscillates in air in the vicinity of (or as it approaches) the surface of the sample, although never contacting the surface. SEM images were taken at a magnification suitable for comparing the morphology of the alloys with topographic features displayed by the AFM images as shown in Figure 7.

2.2 Statistical Analysis

The data collected in this study were processed using the NanoScope V.5.31 data processing software, which is part of the metrology package. Statistical analysis was conducted to assess whether there was any significant difference between the measurements obtained as a result of sample composition, surface treatments, surface measurements, and scan size using a general linear ANOVA model (SPSS v.17). Between subject effects were analyzed using a two-way ANOVA. By assuming normality, the initial exponential modeled data was transformed into a linear model and all data was found to be within two standard deviations from the mean values. Contrasts between subjects were determined and a pair-wise comparison was made between subjects. Bonferroni's post-hoc test was selected as it adjusts degrees of freedom for p-values, and provides insight into data results. Differences with p values less than .05 were considered significant.

3. Results

The topography of twelve ternary Nitinol alloys was analyzed by AFM over four different scan areas within the nanometer to micrometer range. A comparison of surface roughness by RMS and Ra values for scan size III (115× 115 μm) is shown in Figure 1. This scan area represented the largest area over which the topographic analysis was conducted in this study. At this size, most topographical patterns are evident. It can be seen that the RMS values were slightly higher than Ra values for all alloy samples. The RMS and Ra for NiTiCu were slightly higher than that of NiTi, which had the lowest RMS and Ra values for all samples tested within this range. Results also revealed that the RMS and Ra values of NiTiTa-EP were marginally greater than that of NiTi-MEP. The surface area of the alloys was analyzed over this dimensional range where the surface features are dimensionally appropriate for cellular adhesion. The alloys with the lowest surface area were in the order of NiTi, NiTiCr, and NiTiCu with NiTiCu having the lowest value at 13270 nm^2. The surface roughness over the smallest scan size of (800 × 800 nm) is shown in Figure 2, where it can be seen that NiTiCr-MEP had the highest RMS and Ra, while NiTi-MEP had the lowest values amongst all alloys. Surface area results within the nano-scaled dimension of (800 × 800 nm) revealed that NiTiCr-MEP and NiTiCu-MEP distinctly have higher surface areas, as compared with that of the untreated or EP treated alloys. NiTiCr-MEP and NiTiCu-MEP had the highest

RMS, RA and SA values at both the nano-scale and micro-scale dimensions. The determination of mechanical properties for the NiTi alloys with and without MEP and EP surface treatments is summarized in Table 1, which can be compared to the mechanical properties of commercial stents as shown in Table 2. NiTiTa-EP had the greatest standard deviation of ± 16 for the YM. NiTiTa had the lowest YM and SH values of 32 ± 5 GPa, and 1.2 ± 0.2 GPa, respectively. NiTiCr, NiTiCr-EP, and NiTiCr-MEP had YM and SH values that were relatively the same at 98 GPa.

SEM images revealed several distinct patterns for all alloys, which are schematically represented in Figure 3. All untreated alloys (NiTi, NiTiCr, NiTiCu, NiTiTa) revealed a flat morphology and lower Rmax values when compared to the MEP and EP treated alloys. NiTi-MEP and EP were also visually flat. NiTiCr-MEP revealed elevated grain boundaries, while NiTiCr-EP had depressed grain boundaries. Both NiTiCu-MEP and NiTiCu-EP had depressed grain boundaries. NiTiTa-MEP had a flat morphology, while NiTiTa-EP revealed elevated belts which appeared not to be confined at the grain boundaries. NiTi-MEP and NiTiCu-MEP had higher Rmax values when compared with NiTi-EP and NiTiCu-EP, while NiTiTa-MEP was relatively flat. NiTiCr-EP had a higher Rmax value of 1010 nm, as compared with NiTiCr-MEP of 755 nm Rmax value.

EDS analysis revealed an aggregation of ternary elements (Cr, Cu) at grain boundaries in MEP, EP, and untreated ternary alloys (Figure 4). NiTiCr grain regions possessed low weight percentages of the untreated, MEP and EP surfaces (6.05 wt%, 4.43 wt%, and 4.13 wt%, respectively). When grain regions were compared with that of the grain boundaries, Cr weight percentages at grain boundaries increased substantially to 19.81 wt%, 19.25 wt%, and 19.88 wt%, respectively.

Lastly, Ra, RMS, and SA were determined for the interior and exterior surfaces of two commercially available stents UNC-1 and COL-1. As seen in Figure 5, the interior and exterior Ra and RMS of COL-1 were greater than those of UNC-1. Furthermore, the exterior surface of stent COL-1 was rougher than the interior surface. An examination of the surface area of the UNC-1 stent revealed that its interior surface area was greater than that of its exterior surface. A summary of the surface roughness analysis, Ra, RMS, and SA for dimensions I (10 × 10 μm) and II (5 × 5 μm) are shown in Table 3. Three-dimensional AFM images of the inner and outer surfaces of stents UNC-1 and COL-1 for a scan area of at (40 × 40 μm) scan sizes are shown in Figure 6.

Generally, the surface roughness (Ra and RMS) of all alloys increased with either EP or MEP surface treatments at both the nano and micro scale. There was no significant difference in surface area of the treated and untreated alloys at the micro scale. However, there was an appreciable increase in the surface area for the MEP surface treated alloys of NiTiCr-MEP and NiTiCu-MEP at the nano-scale dimension.

3.1 Discussion

Depending upon the methodology used, manufacturing processes and surface finishing techniques greatly influence the performance, integrity and quality of the implantable biomaterial [26, 27]. Of particular importance is the interaction between the biomaterial and its implanted environment. Most important biological responses to an implant are: carcinogenicity, cytotoxicity, inflammatory reaction and coagulation [28].

Human platelet cells are approximately 3.2 – 3.6 μm in diameter and 0.92 - 1.1 μm thick [29]. Cells with these dimensions can easily adhere on the rough surfaces of both the bare metal stent samples and ternary Nitinol alloys as revealed by the RMS values for all specimens at all scan dimensions. Supporting research has shown that the shapes of Rat

Derived Fibroblasts (RFDs) can self-modify according to geometric patterns found on the surface to which they may adhere to. RFDs can modify their shape and orientation down to a threshold value of 100 nm in width and 70 nm in depth, but no cellular accommodation was seen at dimensions less than 35 nm [30]. Dimensions for such surface features are most comparable to the micro-patterned surfaces created by electrochemical surface treatments on the binary and ternary NiTi alloys, which can guide endothelial cell adhesion, growth, and reduce the likelihood of in-stent restenosis [24, 30 - 32]. Determination of an optimum threshold surface roughness value for vascular biomaterials is important, as a surface too rough may rupture the wall of a vessel at the implant-wall interface. This need is essential regardless of whether evaluating a bare metal stent or drug-eluting/polymer coated stent, as both material types will have a significant variation of surface roughness.

A worthy consideration is whether the surface roughness of the implantable material significantly alters the fluid dynamics within the vasculature. The Reynolds number (N_R) which is the ratio of convective inertia force to shear force, is used to characterize different flow patterns within a vessel [33]. Lower N_R values are generally laminar flow patterns, whereas higher N_R values approach turbulent flow. The Reynolds number is influenced by the vessel radius, mean velocity of fluid flow, and the surface roughness of the vessel wall [33]. If an implantable device within the vessel has a high surface roughness, the Reynolds number within proximity of the implant would increase, influencing the transition zone at which fluid flow is changed from being laminar to turbulent. Rougher interior surfaces of an intravascular stent would disrupt the laminar boundary layer creating a region of separation from the streamline flow and the vessel wall or stent surface. Ultimately, as the region of separation increases, turbulent flow would increase, causing the velocity of the fluid in the region of separation to slow down and the pressure within the intima to increase [33]. This would further contribute to vascular ailments. Clinically, such a phenomenon would resemble symptoms of atherosclerotic plaques and artery stenosis; these would be unfavorable effects from intravascular stents with large micro-patterned surfaces.

The presence of deformations on the surface of the material due to precipitate formation caused by the inhomogeneity of the material matrix, causes localized stress points throughout the material. Such precipitates can be heavily seen on the surface of NiTiTa, NiTiTa-MEP and NiTiTa-EP (Figure 7). It has been shown that such stress points strongly influence the different phase transformations for super-elastic materials at different transformation temperatures [34]. The characterized roughness on the ternary NiTi alloys could expectedly influence such phase transformations due to the higher stress fields within the material induced by the electrochemical MEP and EP surface treatments. Such stress points have also been attributed to the change in mechanical properties seen after the MEP and EP surface treatments on the NiTiTa alloys. MEP and EP surface treatments have acted in some instances to increase the surface roughness and surface area as in NiTiCu, and NiTiCr. This is counter-design intention, as these surface treatments are intended to smoothen and reduce the roughness of a material [18-20]. Rmax values between grain and grain boundaries showed an increase for magneto-electropolished samples NiTi-MEP and NiTiCu-MEP, while electropolished samples NiTiCr-EP, and NiTiTa-EP showed an increase in Rmax. This can be attributed to two factors: (1) influence of magnetic field during electrochemical treatment, and (2) thermodynamic preferential dissolution of grains or grain boundaries due to the electrochemical surface treatment. Accumulation of magnetic elements Cu and Cr at grain boundaries produced two different surface morphologies when MEP and EP effects were compared (Figure 3). NiTiCr-MEP produced grain boundaries that were elevated, while in the absence of a magnetic field the NiTiCr-EP revealed grain boundaries that were depressed. However, this was not the case in NiTiCu, which contains a slightly magnetic ternary element that becomes more magnetic when alloyed with Ni. In both cases for NiTiCu, MEP and EP produced grain boundaries that were depressed.

Tantalum being paramagnetic, also reacted to the influence of a magnetic field during the MEP surface treatment and resulted in a much smoother surface for NiTiTa-MEP (590 nm) when compared to that of NiTiTa (1282 nm) and NiTiTa-EP (1699 nm).

RMS values gathered from all alloys at scan dimensions of (115 × 115 μm) are comparable to the RMS values recorded for the interior and exterior surfaces of commercially available stents which were analyzed (Figures 1, 5). Interior surface elevations on the stents were a maximum of 2 μm in depth, which indicated that they have the potential to alter laminar flow patterns once implanted within a vessel (Figure 6). MEP and EP surface treatments on endovascular materials may also disrupt flow regimes within the vessel; however, such grooves will allow for enhanced endothelial cell adhesion preventing in-stent restenosis, and reduce the risk of thrombogenicity [24, 30- 32]. Laminar flow patterns may be re-established once endothelialization of the coronary stent implant is complete.

In Figure 7, (10 × 10 μm) AFM sections were compared to large scaled SEM images showing the general surface features for all of the electrochemically treated alloys. It can be seen that AFM images at the (10 × 10 μm) scan dimensions showed rougher surface textures which were correlated with SEM images. NiTiCr-MEP AFM images show a very rough surface with elevations. This can be compared to its SEM image which shows elevated grain boundaries induced by the MEP surface treatment. Likewise, NiTiCu-MEP, NiTiCu-EP, and NiTiCr-EP AFM images all show the (10 × 10 μm) regions with reduced roughness which can be correlated to depressed grain boundaries as seen in their respective SEM image. NiTiTa-MEP and NiTiTa-EP SEM images both show a high degree of precipitate formation due to the inhomogeneity of Nickel-Titanium-Tantalum. These precipitates can also be seen as cylindrical columns in the (10 × 10 μm) AFM images. NiTiTa and NiTiTa-EP samples also reveal to have the highest Ra and RMS values at the (10 × 10 μm) and (5 × 5 μm) scan dimensions, which has been attributed to the high frequency of surface precipitates (Table 3).

The inhomogeneous multi-phased material formation with NiTiTa has also been attributed to the large change in mechanical properties seen after MEP and EP surface treatments which could potentially lend to a preferential dissolution of grain or grain boundary regions. Likewise, materials with higher Ra and RMS values, affect corrosion parameters such as i_{corr} and E_{corr}, which would effectively increase the corrosion current and free corrosion potential shifts to more positive values, thus increasing the rate of corrosion [35].

YM and SH were determined for all NiTi alloys and are summarized in Table 1. There is a linear relationship between the SH and YM for the values as seen for both the different NiTi alloys and the commercial stents (Table 2). Generally, a higher surface hardness value tends to correlate to a higher YM value. This is a reasonable expectation as explained by Hertzian contact mechanics, which produces a relationship between tip geometry, contact area for tip radius and specimen surface, and the applied load to the indenter [36]. From the nano-indentation testing, the area of contact is determined from the indentation depth and the geometry of the tip [36]. As a load is applied to the surface of the material, the resistant force produces the surface hardness data. The elastic modulus is determined from the elastic recovery phase during the unloading of the indenter from the specimen surface [37]. NiTiTa-EP and NiTiCr, NiTiCr-MEP, and NiTiCr-EP, have higher YM and SH values when compared to other ternary surface treated alloys and NiTi (Table 1). The increase in surface hardness values is most likely due to the presence of ternary elements like Ta and Cr. RMS values tend to be directly proportional with YM and SH values at the (10 × 10 μm) and (5 × 5 μm) scan dimensions for NiTiCr-MEP, NiTiCr-EP, NiTiTa-EP, NiTiCu, NiTiCu-MEP, and NiTiCu-EP. However, because this trend was not consistent amongst all of the data, it is not conclusive. Such variation in data measurements could be attributed to the super-elastic

nature of these materials, as they readily undergo phase transformations at different temperatures. Therefore, the experimental values for YM, SH, as well as Ra, SA, and RMS values reported by AFM testing, might change as environmental temperatures vary leading to some instances where the determination of the mechanical properties for the different binary and ternary alloys may be contradictory [38].

Surface characterization of implantable materials is especially influential for therapies involved in a direct interface with flowing blood. A rough surface promotes faster blood coagulation than a surface that is highly polished [39-40]. Again, this can be explained by regions of blood flow separation. If the interior surface of a stent is rough, there would be a reduction in the velocity of blood in the separated regions of flow causing points of stagnation near the boundary layer on the surface of the implant, thus leading to more blood being coagulated [33]. In this study, it is evident that the addition of copper to Nitinol yielded lower surface roughness and surface area values when analyzed at scan areas of (115 × 115 μm). Such smoother surfaces may lead to reduced corrosion, and reduced risks of thrombosis [41-43].

It should be noted that *in-vitro* and *in vivo* data with materials containing copper, have shown copper's toxicity and role in the mechanism of Alzheimer's disease [44]. While excessive amounts of copper within the body are toxic to cells, the addition of Cu to NiTi has been shown to control the transformation hysteresis which super elastic materials readily undergo [45]. Therefore, material designs including Cu should be strictly controlled. The application of polishing has increased the surface roughness of ternary NiTiCu, relative to the unpolished NiTiCu. Copper's readiness to dissolve from the NiTi matrix provides probable insight into the increased cytotoxicity and poor cell adhesion and activity of Human Fibroblast cells when fixated on NiTiCu as reported during *in-vitro* studies [45]. NiTiCu was the smoothest alloy, while NiTiTa and NiTiTa-EP had the highest RMS values often reaching statistical significance.

Analyzing RMS, SA, and Ra values at scan dimensions of (800 × 800 nm), (5 × 5 μm), (10 × 10 μm), and (115 × 115 μm), provided a conceptualization of cell-to-surface area ratio for possible protein adsorption and cellular binding regions. Scan dimensions at (800 × 800 nm) and (115 × 115 μm) are at the extremes of analysis. RMS and SA data for each analysis dimension greatly vary due to the localized surface roughness. At (115 × 115 μm), scans were made to evaluate a broader scope of the surface, which would account for the micrometer changes in vertical displacement between the grains and the elevated or depressed grain boundaries due to the MEP and EP surface treatments. RMS values gathered from the (800 × 800 nm) scan dimension are more representative of a protein binding site, which is small enough to be measured on the surface of an elevated or depressed grain boundary, or on the surface of the grain itself [1]. In Figure 4, it can be seen that the surface area is higher for the (800 × 800 nm) scan dimension as compared to the (115 × 115 μm) scan dimension.

This can be explained by the RMS measurement of surface roughness. In the (115 × 115 μm) scan dimension, the variability of roughness is much higher because the difference between high and low regions on the surface is greater, but fails to translate into a larger surface area (Figure 11-A). Rather, if the variability of surface roughness is less, but the frequency of variance is higher, then a region with a higher surface area would result as seen from analysis at the (800 × 800 nm) scan dimension (Figure 11-B).

4. Conclusions

Atomic force microscopy provides a powerful tool for analyzing the surface of alloys at the micrometer and sub-micrometer scale. In terms of the biocompatibility of an implant, such

analysis allows for predictive inferences on the interaction between the implant surface, blood proteins, and cellular interactions. Results from experimentation revealed a positive correlation between surface roughness and available surface area. Reported RMS values were nearly always higher than surface roughness (Ra) values for all alloys, except in the case of NiTiCu-EP. EP and MEP treated alloys had higher RMS values in scan dimensions I, II, III, and IV. Alloys without MEP or EP surface treatments exhibited a flat 2-D profile, while NiTiCu showed depressed grain boundaries relative to grain regions after MEP and EP treatments, and NiTiCr-MEP showed elevated grain boundaries when compared with that of NiTiCr-EP. EDS analysis revealed an accumulation of ternary elements (Cr, Cu) at the grain boundaries in substantial amounts, while grain regions contained minimal weight percentages. MEP surface treatments were effective in increasing surface roughness for ternary alloys with magnetic elements like Cu and Cr, whereas EP surface treatments were marginally less effective on binary and ternary Nitinol alloys without a magnetic ternary element. Ternary NiTiCr with/without MEP and EP were tested to be more consistent than other alloys, as roughness measurements were consistently higher, independent of scan dimension, and elemental phase separation was minimal. NiTiCr alloys developed well-defined elevated grain boundaries with an MEP surface treatment and depressed grain boundaries with an EP surface treatment, thus creating a micro-patterned surface in favor of accelerated endothelialization, reducing the likelihood of post-treatment in-stent restenosis and thrombosis.

Acknowledgments

D.P. supported by NIH/NIGMS R25 GM061347. The project described was supported by Award Number SC3GM084816 from the National Institute of General Medical Sciences. Dharam Persaud (D.P.) would also like to thank Mr. Neal Ricks, and Mr. Jenai Alexis for their effort in assisting with this study.

References

1. Covani U, Giacomelli L, Krajewsky A, Ravaglioli A, Spotorno L, Loria P, Das S, Nicolini C. Biomaterials for orthopedics: A roughness analysis by atomic force microscopy. Journal of Biomaterials Research Part A. 2007; 82:723–730.
2. Van den Beucken JJJ, Vos MRJ, Thüne PC, Hayakawa T, Fukushima T, Okahata Y, Walboomers XF, Sommerdijk NAJM, Nolte RJM, Jansen JA. Fabrication, characterization and biological assessment of multilayered DNA-coatings for biomaterial purposes. Biomaterials. 2006; 27:691–701. [PubMed: 16076484]
3. Kasemo B, Gold J. Implant surfaces and interfaces processes. Advances in Dental Research. 1999; 13:8–20. [PubMed: 11276751]
4. Haider W, Munroe N, Pulletikurthi C, Gill PK, Amruthaluri S. A comparative biocompatibility analysis of ternary nitinol alloys. Journal of Materials Engineering and Performance. 2009; 8:760–764. [PubMed: 19956791]
5. Kanchibhotla S, Munroe N, Kartikeyan T. Amorphization in Ni-Ti-Ta systems through mechanical alloying. Journal of Material Science. 2005; 40:5003–5006.
6. Mehta A, Gong X-Y, Imbeni V, Pelton AR, Ritchie RO. Understanding the Deformation and Fracture of Nitinol Endovascular Stents Using *In Situ* Synchrotron X-ray Microdiffraction. Advanced Materials. 2007; 19:1183.
7. Shabalovskaya SA. Surface corrosion and biocompatibility aspects of nitinol as an implant material. Bio-Medical Material Engineering. 2002; 12:69–109.
8. Haider, Waseem. FIU Electronic Theses and Dissertations. 2010. Enhanced biocompatibility of NiTi via surface treatment and alloying. Paper 177
9. Nam TH, Saburi T, Nakata T, Shimizu K. Shape memory characteristic and lattice deformation In Ti-Ni-Cu alloys. Materials Transactions. 1990; 31:1050–1056.
10. Fukuda, Kakeshita T, Kitayama M, Saburi K. Effect of ageing on martensitic transformation in a shape memory Ti40.5Ni10Cu alloy. Journal de Physique IV. 1995; 5:C8–717.

11. Wakhloo A, Tio F, Lieber B, Schellhammer F, Grad M, Hopkins L. American Journal of Neuroradiology. 1995; 16:1043–1051. [PubMed: 7639126]
12. Cura M, Sprague E. Bare Stent Technology and its Utilization in the Treatment of Atherosclerotic Obstructive Disease. Vascular Disease Management. 2010; 7:95–102.
13. Letourneau-Guillon L, Soulez G, Beaudoin G, Olivia XL, Giroux MF, Qin Z, Boussion N, Therasse E, De Guise J, Cloutier G. CT and MR imaging of Nitinol stents with radiopaque distal markers. Journal of Vascular Interventional Radiology. 2004; 15:614–624.
14. Baboian R. Corrosion tests and standards: application and interpretation. ASTM International (2). 2005; 20:585–882.
15. Strecker EP, Liermann D, Barth KH. Expandable tubular stents for treatment of arterial occlusive diseases: experimental and clinical results. Radiology. 1990; 175:97–102. [PubMed: 2315509]
16. Shabalovskaya SA. International Materials Review. 2001; 45:233–250.
17. Vander Voort GF. Chemical and electrolytic polishing, ASM Handbook, metallography and microstructures. ASM International. 2004; 9:281–293.
18. Hanke L, Bayha E. Surface characterization for optimizing electropolishing for medical devices. Medical device materials: proceedings of the materials & processes for medical devices conference. 2004:81–86.
19. Hryniewicz, T.; Rokicki, R.; Rokosz, R. Proceedings of 16th International Conference on Metallurgy and materials, Symposium D, Surface Engineering, D2. Hradec nad Moravici, Czech Republic: Tangers; 2007. Metal surface modification by magneto-electro polishing; p. 1-8.
20. Rokicki, R. Apparatus and method for enhancing electropolishing utilizing magnetic Fields U S Patent Application. 2,006,124,472. 2006.
21. Palmaz JC, Benson A, Sprague EA. Influence of surface topography on endothelialization of intravascular metallic material. Journal of Vascular Interventional Radiology. 1999; 10:439–444.
22. Hryniewicz T, Rokicki R, Rokosz K. Corrosion characteristics of medical-grade AISI type 316L stainless steel surface after electropolishing in a magnetic field. Corrosion. 2008; 64:660–666.
23. Valois CRA, Silva LP, Azevedo RB. Atomic force microscopy study of stainless-steel and nickel-titanium files. Journal of Endodontics. 2005; 31:882–885. [PubMed: 16306823]
24. Ranjan A, Webster T. Increased endothelial cell adhesion and elongation on micro-patterned nano-rough poly(dimethlysiloxane) films. Nanotechnology. 2009; 30:305102. [PubMed: 19581692]
25. Tsapikouni T, Missirlis Yannis. Protein-Materials Interactions: From micro-to-nano scale. Material Science and Engineering: B. 2008; 152:2–7.
26. Gadelmawla ES, Koura MM, Maksoud TMA1, Elewa IM, Soliman HH. Roughness parameters. Journal of Materials Processing Technology. 2002; 123:133–145.
27. Schetky, LMcD; Wu, MH. Issues in the further development of Nitinol properties and processing for medical device applications. Memry Corporation; Bethel, Connecticut, USA:
28. Oeveren, W Van; Maijers, P Schoen; Van Boven, SH. Hemocompatibility of Stents. Progress of Biomaterials. 1999; 4:17–22.
29. Inglis D, Morton K, Davis J, Zieziulewicz TJ, Lawrence D, Austin R, Sturm J. Microfluidic device for label-free measurement of platelet activation. Lab chip. 2008; 8:925–931. [PubMed: 18497913]
30. Loesberg WA, Riet J te, van Delft FCMJM, Schön P, Figdor CG, Speller S, van Loon JJWA, Walboomers XF, Jansen JA. The threshold at which substrate nanogroove dimensions may influence fibroblast alignment and adhesion. Biomaterials. 2007; 27:3944–3951. [PubMed: 17576010]
31. Santos MI, Pashkuleva C, Alves ME, Gomes S, Fuchs R, Unger E, Reis RL, Kirkpatrick CJ. Surface-modified 3D starch-based scaffold for improved endothelialization for bone tissue engineering. Journal of Materials Chemistry. 2009; 19:4091–4101.
32. Shen Y, Wang G, Chen L, Li H, Yu P, Bai M, Zhang Q, Lee J, Qingsong Y. Investigation of endothelialization on biomedical nitinol (NiTi) alloys: Effects of surface micropatterning combined with plasma nanocoatings. Acta Biomaterialia. 2009; 5:3593–3604. [PubMed: 19477302]
33. Fung, YC. Biomechanics Circulation. 2. 1996. p. 134-200.

34. Chumlyakov, Yu I.; Panchenko, E Yu; Kireeva, IV.; Shaporov, DA.; Aksenov, VB.; Sehitoglu, H.; Karaman, I.; Gall, K.; Maier, H. Shape memory and super-elasticity in nickel-titanium single crystals aged under applied stress. Journal De Physique. 2003; 112:799–802.
35. Mourad MY, Kandeil AY. Influence of Surface Finish Parameters on Corrosion of Zinc. Qatar Univ. Science Bulletin. 1989; 9:65–77.
36. Johnson, KL. Contact Mechanics. 1. Cambridge University Press; New York: 1987. p. 84-105.
37. Mencin, P.; Van Tyne, CJ. FIERF. Department of Metallurgical and Materials Engineering; A method for measuring the hardness and elastic modulus of the surface layer on hot forging dies using a nano indentation; p. 1-13.
38. Alavi S, Raji S, Ghorbani A. Effects of steam and dry-heat sterilization on bending of NiTi wires. Orthodontic Waves. 2009; 68:123–128.
39. Hanson, SR.; Harker, LA. Biomaterials science: an introduction to materials in medicine. Academic Press; San Diego, USA: 1996. Blood coagulation and blood-materials interaction; p. 193-199.
40. Harker, La; Rainer, BD.; Didisheim, P. Cardiovascular biomaterials and biocompatibility: a guide to the study of blood-tissue-material interactions. Elsevier; New York: 1993.
41. Gutensohn K, Beythien C, Koester R, et al. In vitro biocompatibility analyses of stents coated with diamond-like carbon by flow cytometery, cell growth assays and electron microscopy. Infusion Therapy and Transfusion Medicine. 2000; 27:200–206.
42. Gutensohn K, Beythien C, Bau J, et al. In vitro analyses of diamond-like carbon coated stents: reduction of metal ion release, platelet activation, and thrombogenicity. Thrombosis Research. 2000; 99:577–585. [PubMed: 10974344]
43. Koster R, Vieluf D, Kiehn M, et al. Nickel and Molybdenum contact allergies in patients with coronary in stent-restenosis. Lancet. 2000; 356:1895–1897. [PubMed: 11130387]
44. Quinn JF, Crane S, Harris C, Wadsworth TL. Copper in Alzheimer's disease: too much or too little? Expert Review of Neurotherapeutics. 2009; 9:631–637. [PubMed: 19402774]
45. Gil FJ, Solano E, Pena J, Engel E, Mendoza A, Planell A. Microstructural, mechanical and cytotoxicity evaluation of different NiTi and NiTiCu shape memory alloys. Journal of Materials Science: Materials in Medicine. 2004; 15:1181–1185. [PubMed: 15880925]

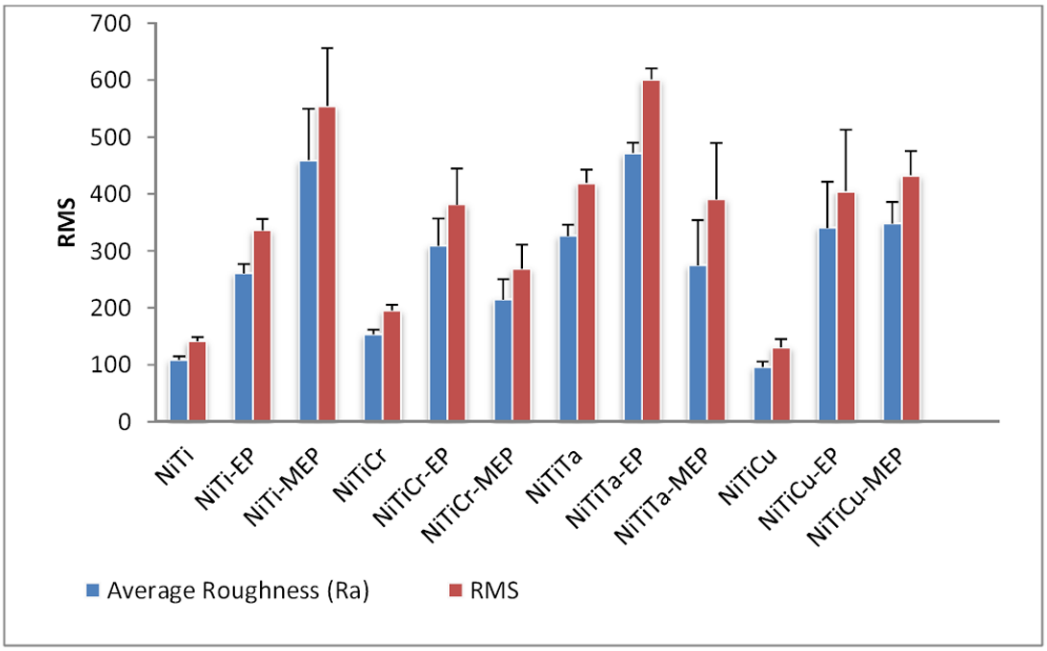

Figure 1.
Surface roughness (nm) and RMS values of Nitinol alloys, scan size III 115 × 115 μm (Average of five tests).

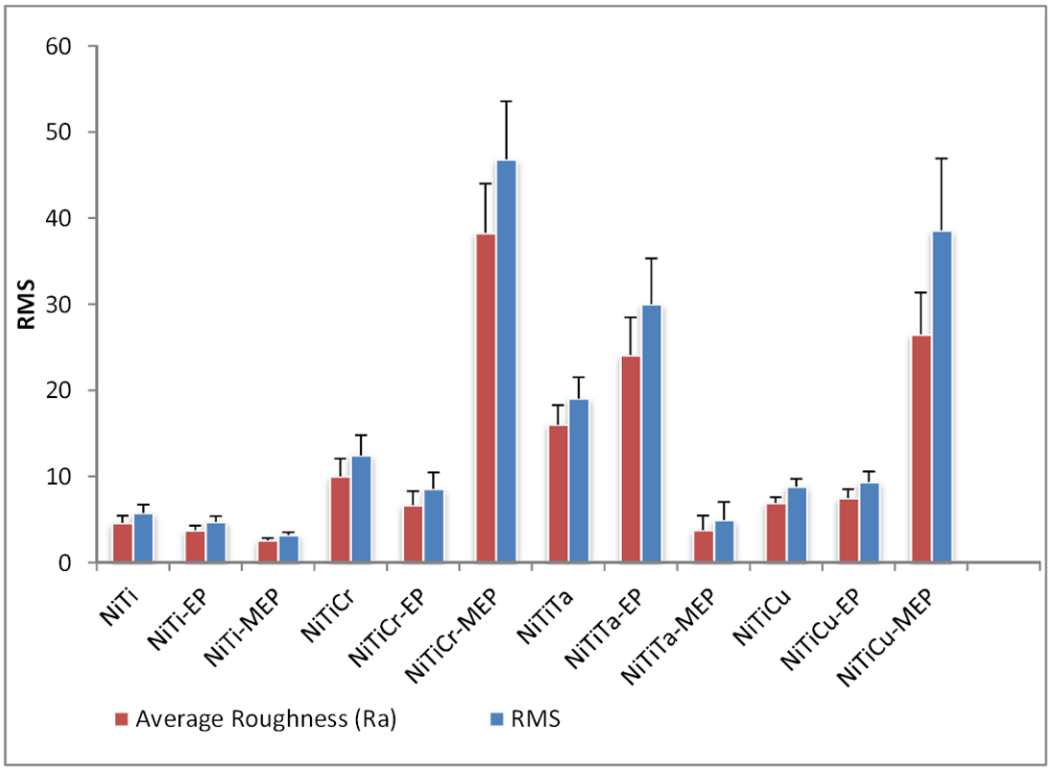

Figure 2.
Surface roughness (nm) and RMS values of Nitinol alloys, scan size IV 800 × 800 nm (Average of ten tests).

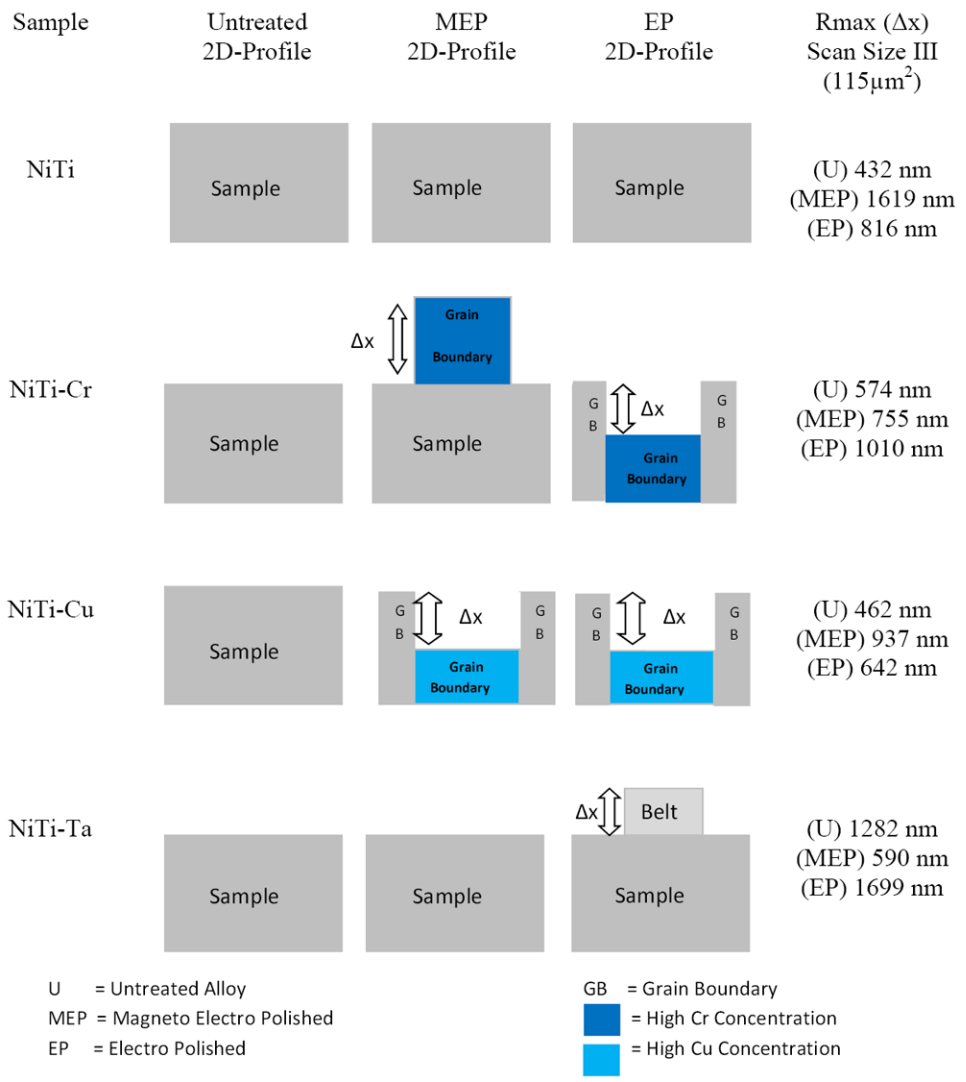

Figure 3.

2-Dimensional schematic illustrating surface patterns of elevated and depressed grain boundaries and grains for different alloy compositions with MEP and EP surface treatments. Rmax is the height difference between the highest and lowest points within the image.

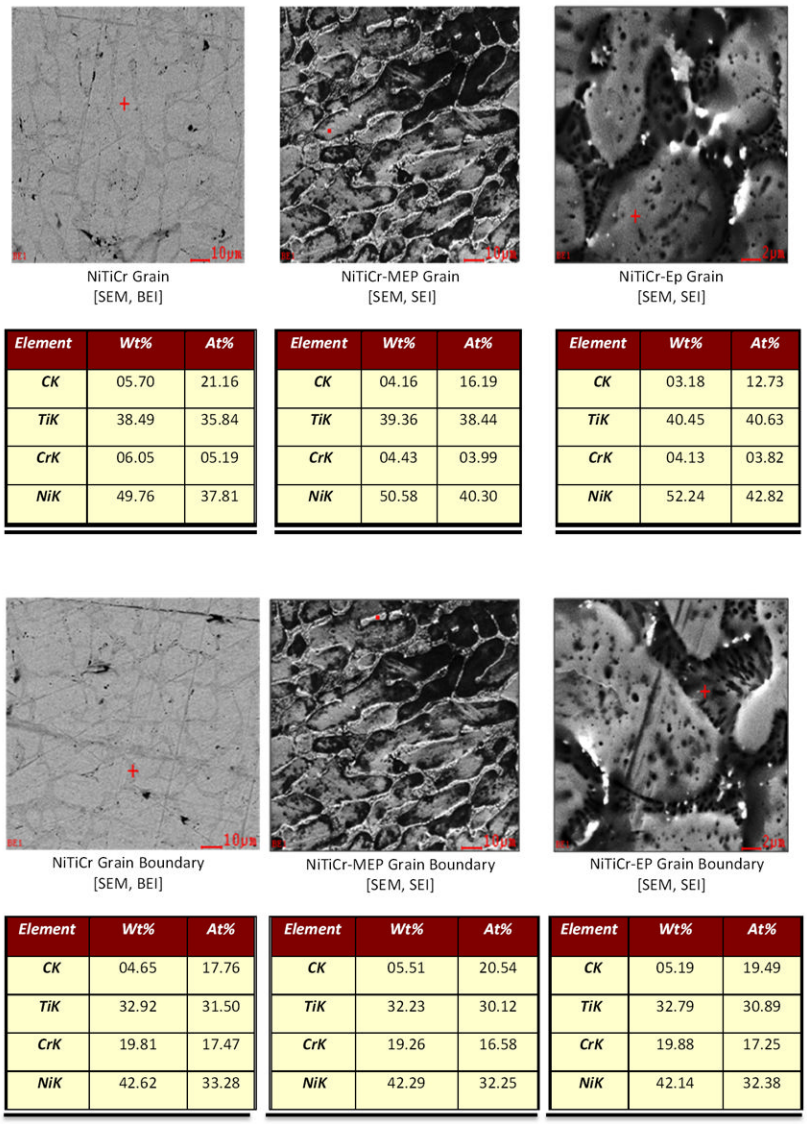

Element	Wt%	At%
CK	05.70	21.16
TiK	38.49	35.84
CrK	06.05	05.19
NiK	49.76	37.81

Element	Wt%	At%
CK	04.16	16.19
TiK	39.36	38.44
CrK	04.43	03.99
NiK	50.58	40.30

Element	Wt%	At%
CK	03.18	12.73
TiK	40.45	40.63
CrK	04.13	03.82
NiK	52.24	42.82

Element	Wt%	At%
CK	04.65	17.76
TiK	32.92	31.50
CrK	19.81	17.47
NiK	42.62	33.28

Element	Wt%	At%
CK	05.51	20.54
TiK	32.23	30.12
CrK	19.26	16.58
NiK	42.29	32.25

Element	Wt%	At%
CK	05.19	19.49
TiK	32.79	30.89
CrK	19.88	17.25
NiK	42.14	32.38

Figure 4.
SEM and EDS analysis showing accumulation of Cr at grain boundaries in MEP, EP, and untreated alloys. Red Crosshair is the point of analysis.

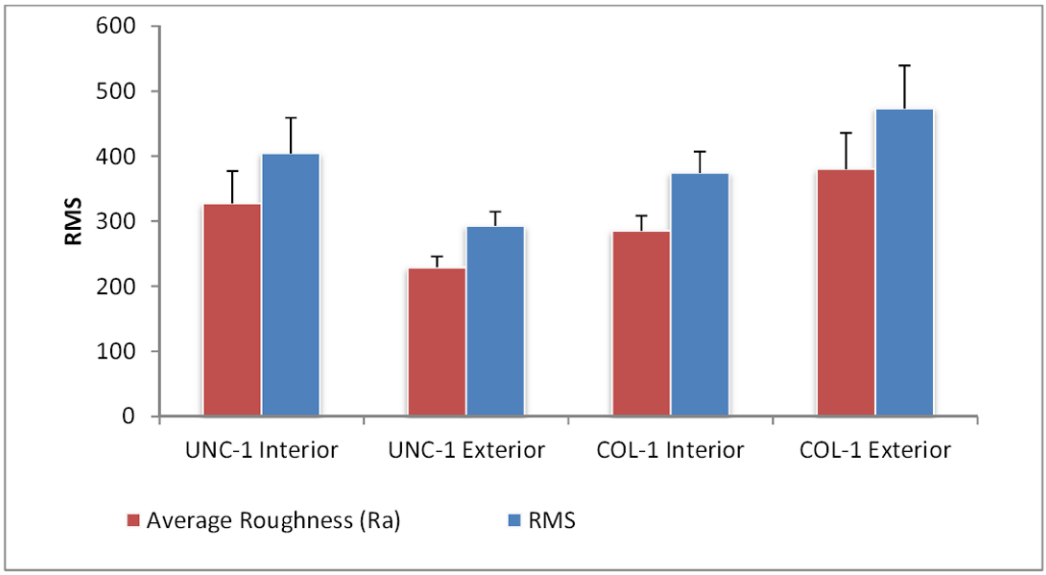

Figure 5.
Surface roughness (nm) and RMS values on the interior and exterior surfaces of Nitinol stents.

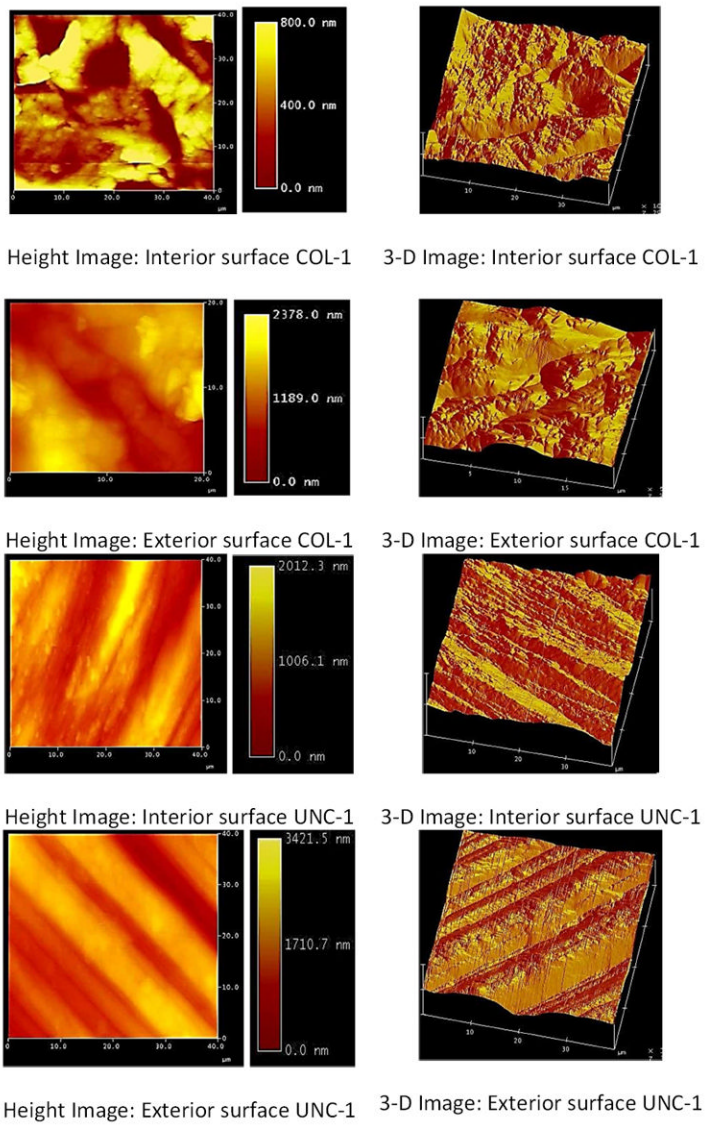

Figure 6.
AFM images of interior and exterior surfaces of cardiovascular stents.

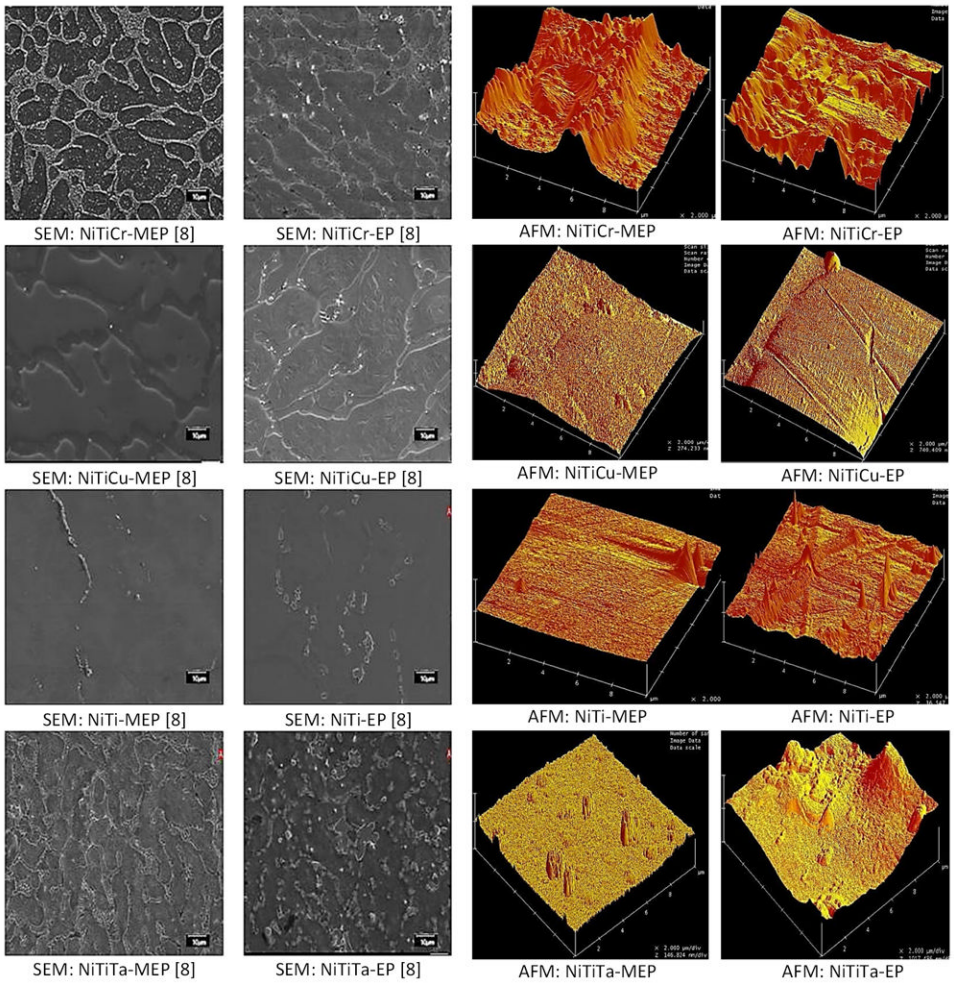

Figure 7.
SEM and AFM Images of EP and MEP surface treated Nitinol alloys (AFM scan size 10 × 10 μm).

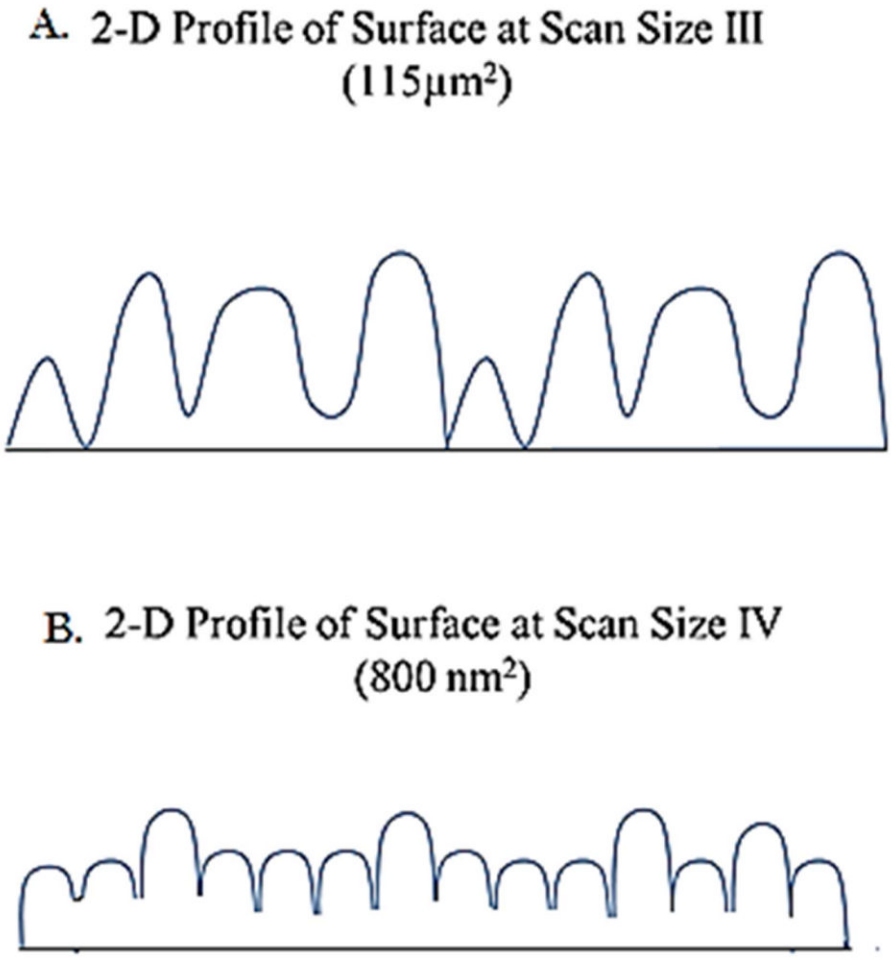

Figure 8.
Schematic 2-dimensional profiles for alloy surfaces at different scanning sizes illustrating variation in surface roughness. A) Shows greater variability in surface roughness, with a lower surface area. B) Shows reduced surface roughness variability, with an overall higher surface area due to increased frequency of variation.

Table 1

Mechanical properties of MEP and EP surface treated binary and ternary Nitinol alloys

Sample	Young's Modulus GPa	Surface Hardness GPa
NiTi	73 ± 3	4.5 ± 0.2
NiTi-EP	61 ± 3	4.2 ± 0.1
NiTi-MEP	69 ± 3	4.5 ± 0.2
NiTiCu	65 ± 8	3.0 ± 0.8
NiTiCu-EP	76 ± 3	3.8 ± 0.1
NiTiCu-MEP	75 ± 2	5.3 ± .02
NiTiTa	32 ± 5	1.2 ± 0.2
NiTiTa-EP	97 ± 16	5.7 ± 1.5
NiTiTa-MEP	62 ± 2	3.8 ± 0.2
NiTiCr	98 ± 5	6.2 ± 0.7
NiTiCr-EP	98 ± 9	6.5 ± 0.7
NiTiCr-MEP	91 ± 6	5.9 ± 0.3

Table 2

Mechanical properties of cardiovascular stents

Stent Sample	Young's Modulus GPa	Surface Hardness GPa
COL-1	69 ± 7	5 ± 0.6
UNC-1	65 ± 3	4.5 ± 0.3

Table 3

Surface roughness and surface area measurements of Nitinol alloys, scan size I, 10× 10 μm and scan size II, 5 × 5 μm

	Size I (10 × 10 μm)			Size II (5 × 5 μm)		
	Surface Roughness [nm]	**RMS**	**Surface Area [nm^2]**	**Surface Roughness [nm]**	**RMS**	**Surface Area [nm^2]**
NiTiCr-EP	176 ±34	225 ± 33	131 ± 14	122 ± 56 *	155 ± 63 *	37 ± 10
NiTiCr-MEP	85 ± 14	111 ± 11	108 ± 9	66 ± 24	83 ± 29	27 ± 2
NiTiCr	47 ± 10	60 ± 15	101 ± 1	38 ± 19	48 ± 28	26 ± 1
NiTiCu-EP	100 ± 5	130 ± 6	105 ± 4	86 ± 84	75 ± 56	29 ± 9
NiTiCu-MEP	100 ± 23	127 ± 28	120 ± 25	59 ± 25	76 ± 33	33 ± 13
NiTiCu	62 ± 30	80 ± 40	102 ± 2	25 ± 7	32 ±10	26 ± .05
NiTi	66 ± 20	81 ± 28	101 ± .24	37 ± 21	40 ± 26	40 ± 44
NiTi-EP	25 ± 10	37 ± 18	110 ± 9	34 ± 33	49 ± 48	27 ± 2
NiTi-MEP	31 ± 31 *	46 ± 44	113 ± 23	22 ± 20	45 ± 70	28 ±5
NiTiTa	273 ± 69 *	345 ± 68 *	125 ± 26	172 ± 74 *	215 ± 92 *	29 ± 3
NiTiTa-EP	241 ± 98 *	300 ± 126 *	110 ± 6	169 ± 92 *	217 ± 111 *	29 ± 4
NiTiTa-MEP	32 ± 20	47 ± 33	104 ± 5	24 ± 38	34 ± 49	27 ± 4